
Controlling the deformation space of soft membranes using fiber reinforcement

©The Author(s) 2020
DOI:
10.1177/0278364919897134

Nick Sholl^{1,3*}, Austin Moss^{1,3*}, Mike Krieg^{1,3}, and Kamran Mohseni^{1,2,3}

Abstract

Recent efforts in soft-body control have been hindered by the infinite dimensionality of soft bodies. Without restricting the deformation space of soft bodies to desired degrees of freedom, it is difficult, if not impossible, to guarantee that the soft body will remain constrained within a desired operating range. In this paper, we present novel modeling and fabrication techniques for leveraging the reorientation of fiber arrays in soft bodies to restrict their deformation space to a critical case. Implementing this fiber reinforcement introduces unique challenges, especially in complex configurations. To address these challenges, we present a geometric technique for modeling fiber reinforcement on smooth elastomeric surfaces and a two-stage molding process to embed the fiber patterns dictated by that technique into elastomer membranes. The variable material properties afforded by fiber reinforcement are demonstrated with the canonical case of a soft, circular membrane reinforced with an embedded, intersecting fiber pattern such that it deforms into a prescribed hemispherical geometry when inflated. It remains constrained to that configuration, even with an additional increase in internal pressure. Furthermore, we show that the fiber-reinforced membrane is capable of maintaining its hemispherical shape under a load, and we present a practical application for the membrane by using it to control the buoyancy of a bioinspired autonomous underwater robot developed in our lab. An additional experiment on a circular membrane which inflates to a conical frustum is presented to provide additional validation of the versatility of the proposed model and fabrication techniques.

Keywords

soft robotics, fiber reinforcement, bioinspiration, soft composites, passive deformation control

1 Introduction

The advantages of soft robots have rapidly been gaining the attention of the robotics community, as evidenced by this journal's special edition, among others. Their appeal lies in the ability of compliant bodies and components to offer more robust and adaptable performance than traditional rigid systems. Flexible robotic structures are less prone to critical failure, as they can deform to accommodate critical loads while maintaining the ability to return to an operational state (Trivedi, Rahn, Kier and Walker 2008; Rus and Tolley 2015; Manti, Cacucciolo and Cianchetti 2016; Laschi, Mazzolai and Cianchetti 2016). Similarly, a deformable body can collapse down to fit through narrow openings in order to reach normally inaccessible locations. When it comes to tasks like grasping and tactile sensing, a compliant manipulator allows for a much more sensitive touch by deforming to fit the geometry of objects (Polygerinos, Correll, Morin, Mosadegh, Onal, Petersen, Cianchetti, Tolley and Shepherd 2017; Galloway, Becker, Phillips, Kirby, Licht, Tchernov, Wood and Gruber 2016). Soft skins have shown tremendous promise as sensors and tools for haptic feedback (Tavakoli, Rocha, Lourenço, Lu and Majidi 2017). Soft robotic elements are also inherently safer for human-robot interactions, or for robots studying and manipulating sensitive biological systems. For a review of the current state of the art in soft robotic systems please refer to Trivedi, Rahn, Kier and Walker (2008); Rus and Tolley (2015); Manti,

Cacucciolo and Cianchetti (2016); Laschi, Mazzolai and Cianchetti (2016).

Deformable robotic platforms allow for a level of versatility and adaptability unrivaled by rigid systems, which could be integral to the next generation of intelligent, adaptable robots (Trivedi, Rahn, Kier and Walker 2008). Traditional robotic systems are built with a series of rigid elements connected through different types of joints, thus having a finite number of degrees of freedom (DOFs) defining the system configuration. An elastic body, on the other hand, can deform to desired shapes, having an infinite number of DOFs associated with a continuous deformation space. This increase in versatility comes with additional challenges, however, associated with actuation and structural stability. For rigid robots, a single, high-strength actuator can be applied to each DOF to provide complete control authority

University of Florida, Gainesville

¹Department of Mechanical and Aerospace Engineering

²Department of Electrical and Computer Engineering

³Institute for Networked Autonomous Systems

*These authors contributed equally to this work.

Corresponding author:

Kamran Mohseni

University of Florida,

Department of Mechanical and Aerospace Engineering,

Gainesville, FL 32611

USA

Email: mohseni@ufl.edu

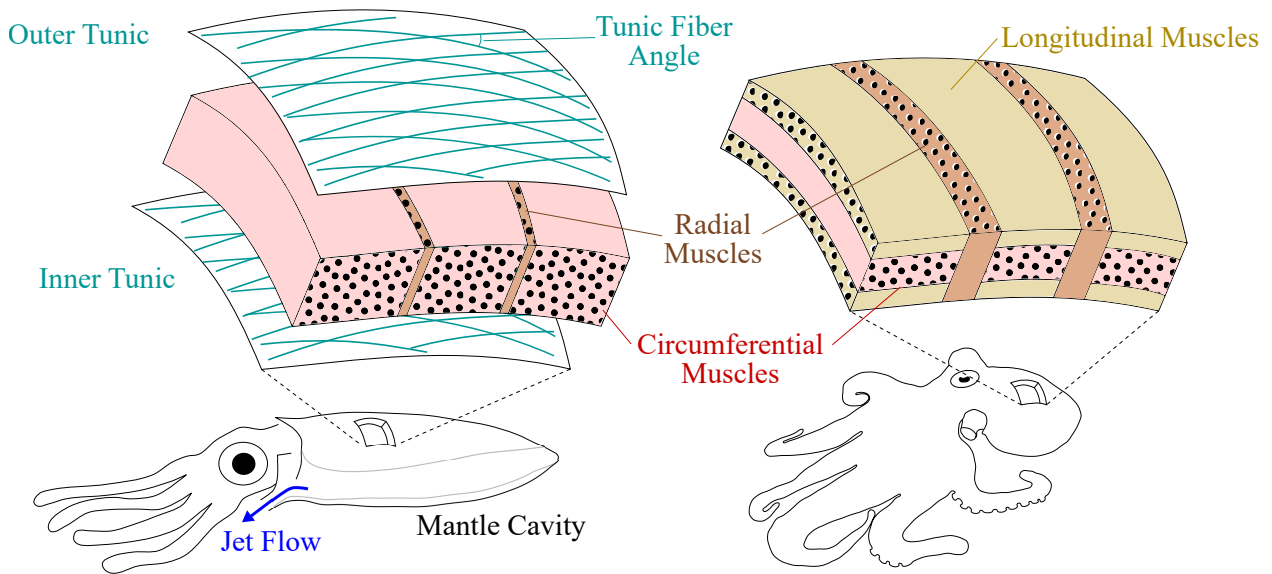


Figure 1. Schematics of squid mantle tissue dominated by circular muscle fibers with both inner and outer tunics (left) and octopus mantle tissue with circular, radial, and longitudinal muscle tissue (right).

over that DOF. If a traditional actuator is applied to a flexible body, however, it will often only cause local deformation at the location where the force/torque is applied. Furthermore, the robot will likely be subjected to external loading during operation, which may cause undesired deformation. Therefore, soft robots and systems require novel distributed actuation and sensing techniques for proper operation.

Many researchers in the soft robotic community have sought inspiration for these new techniques from systems already found in nature, since biological systems have learned to successfully incorporate compliant elements, including soft structures with no rigid elements whatsoever. There is a class of biological structures, without rigid support, known as muscular hydrostats (Kier 1992). Muscular hydrostats are structures composed of interwoven muscle fibers which provide both actuation and structural support in three-dimensional space. These structures include elephant trunks, mammalian tongues, and cephalopod mantles, arms, and tentacles, to name a few. Muscular hydrostats serve as an excellent model for the possible realizations of soft robotic components, but octopus and squid mantles, in particular, help to illustrate how fiber reinforcement can be utilized to control the deformation space of soft bodies.

The mantle is a muscular hydrostat that extends like a hood over cephalopods and creates an internal fluid cavity used for jet propulsion. The octopus mantle is composed of three orthogonal muscle groups, namely radial, longitudinal, and circumferential (Gosline and DeMont 1985). Figure 1 shows a section of the octopus mantle and the different muscle groups. The octopus mantle is amazingly versatile, allowing it to perform jetting, enlarge to scare predators, and even squeeze through openings much smaller than the octopus body size (Mather, Anderson and Wood 2010); in fact, the size of a hole an octopus can squeeze through is only limited by its rigid beak. The squid mantle, though similar, is encased on either side by an array of helical, interwoven, inextensible collagen fibers known as tunics, as depicted in Figure 1. The angle between fibers in squid

tunics is surprisingly consistent, even across different species (Ward and Wainwright 1972; Wainwright, Biggs, Currey and Gosline 1976). The inextensibility of the tunic fibers couples strains in the circumferential and longitudinal directions, effectively reducing the deformation space of the squid mantle to a family of cylindrical shells. We have shown that within this limited deformation space, tunic fiber angles observed in squid maximize the propulsive jet volume flux for a given circumferential contraction (Krieg and Mohseni 2012). The limited deformation space also allows squid to prioritize muscle groups. Since the deformation of the squid mantle in the axial direction is limited by the tunic fibers, it does not require longitudinal muscle groups to oppose this extension. As a result, more of the muscle in the mantle can be dedicated to the circular muscle groups, providing more power to contract the mantle and expel a jet with higher velocity (Bone, Pulsford and Chubb 1981). This specialized mantle structure gives squid impressive jetting capabilities, resulting in the fastest swimming speeds of any marine invertebrate (O’Dor and Webber 1991; Anderson and Grosenbaugh 2005).

In the context of this paper, the two mantle structures (Figure 1) exemplify how fiber reinforcement in soft structures creates a trade-off between versatility and increased performance of a specialized action. Various groups have exploited fiber-reinforcement techniques to accomplish similar goals. Cacucciolo, Renda, Poccia, Laschi and Cianchetti (2016) use fiber reinforcement to create a nonlinear, bending fluidic actuator, focusing on using the fiber-reinforcement to maximize bending angle. Fiber-reinforcement has been used in dielectric actuators to restrict deformation in one direction and improve actuation along the planar direction perpendicular to the fibers (Lu, Huang, Jordi, Kovacs, Huang, Clarke and Suo (2012); Shian, Bertoldi and Clarke (2015)). Huang, Lu, Zhu, Clarke and Suo (2012) created a fiber-reinforced cylindrical dielectric elastomer actuator (DEA) that restricts circumferential expansion to improve axial actuation strains. Bolzmacher, Biggs and Srinivasan (2006)

use fiber reinforcement to maintain prestrain in a wearable DEA. Fabrics have been used as dense fiber meshes in pneumatic actuators (Cappello, Galloway, Sanan, Wagner, Granberry, Engelhardt, Haufe, Peisner and Walsh 2018) and synthetic, 3D camouflaging skins which can inflate to various predefined shapes (Pikul, Li, Bai, Hanlon, Cohen and Shepherd 2017). Some fiber-reinforcement schemes have been used to produce twisting deformations (Ceron, Cohen, Shepherd, Pikul and Harnett 2018; Fang, Pence and Tan 2011).

These studies have almost exclusively used fiber reinforcement to prevent deflection along the axes of the fibers, only scratching the surface of the passive control over deformation that can be achieved with customized fiber reinforcement. In contrast to the fiber reinforcement techniques presented in the literature, we propose creating arrays of intersecting fibers such that any deformation within the plane of those arrays requires fiber reorientation, resulting in a coupling of orthogonal components of strain, similar to the effect of fibers in the squid mantle, that can be tailored to any desired relative strain relationship. The end result is the ability to create nearly any desired space of possible deformations, both increasing desired output for a given actuation and allowing soft actuator density to be weighted toward a desired specialized action, since antagonistic actuation forces are not needed to prevent unwanted deformation. As an additional benefit, the custom arrays of reinforcing fibers also result in highly nonlinear stress-strain (stiffness) relationships in soft composite structures that can be customized for given robotic applications to increase structural stability in a final desired configuration.

Typical investigations into modeling the effect of fiber reinforcement on elastomers focus on determining the material properties at a macroscopic scale, similar to the approach used for calculating material properties in composites (Agarwal and Broutman 1980). Lou and Chou (1988, 1990) use a strain energy approach for Eulerian and Lagrangian strains. Clark (1987) discusses a bimodular approach to modeling zig-zag fibers. Peel (1998) uses experimentally determined material properties to model the stress-strain characteristics without directly characterizing the fiber reorientation's effect on the results. In general, these studies consider the composite to be a single homogeneous material with a highly nonlinear elastic modulus, due to fiber reorientation, and then characterize that modulus empirically.

Krieg and Mohseni (2017) took a different approach to modeling highly-flexible planar composites by treating the fibers and elastomeric matrix as independent systems that interact through a local stress balance directly affected by fiber orientation. This allowed the nonlinear elastic modulus of the combined system to be calculated with high accuracy over a large range of deformation. It was experimentally shown that custom fiber reinforcement increased planar expansion in a desired direction to 14 times that of an unreinforced sample for an equivalent compression of the thickness, which has the ability to drastically improve the performance of soft actuators like DEAs. The analytical stress-strain model was used to simulate energetics in the soft structure, showing a reduction in required deformation work

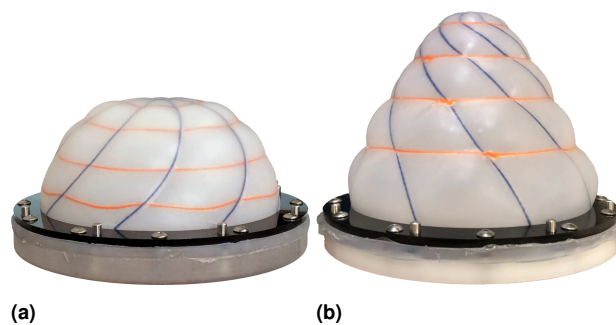


Figure 2. Fiber-reinforced membranes designed to inflate to a hemisphere (a) and a conical frustum (b).

by as much as 83% for optimal fiber configurations and a high modulus ratio compared to no reinforcement or parallel reinforcing fibers.

In this study, we extend the analysis for passive deformation control beyond the planar case and present a technique for using custom arrays of reinforcing fibers to control the 3D deformation space of a soft, elastomer membrane. We develop a technique for modeling the effect of fiber reinforcement on soft membranes, demonstrate the improvements in geometric stability of a fiber-reinforced membrane over that of an unreinforced membrane, subject them both to various loads to evaluate their behavior, validate the model for the simple cases of inflated spheres and conical frustums (Figure 2), and use a fiber-reinforced membrane to aid in the buoyancy control of an autonomous underwater vehicle (AUV) developed in our lab (Krieg, Klein, Hodgkinson and Mohseni 2011; Krieg and Mohseni 2010). This platform has been used regularly in our group as a technology demonstrator (Krieg, Nelson, Eisele and Mohseni 2018) and testing platform to analyze different AUV control strategies and novel distributed sensing techniques (Krieg, Nelson and Mohseni 2019). Interestingly, the AUV also uses a bioinspired jetting propulsion system (Krieg and Mohseni 2008) that utilizes flexible internal cavities that are reinforced with helical metallic fibers to prevent unwanted radial expansion during the pulsation cycles. Similar techniques could be used in a variety of other applications, including improving soft actuator performance, creating soft pumps and valves, enabling advanced haptic feedback, or reducing the complexity of packing the airbags used in cars or to soften the landing of Mars rovers.

We begin by presenting our model of fiber geometry in Section 2, followed by a description of the fabrication process of the fiber-reinforced membranes designed after that model in Section 3. The experiments designed to test the validity of our modeling and the robustness of our fabrication technique are then presented in Section 4, and their results are reported in Section 5. Finally, we discuss the implications and intricacies of our findings in Section 6 and conclude with Section 7.

2 Modeling

Following the methods presented by Krieg and Mohseni (2017), who solved the kinematics of fiber-reinforced elastomeric sheets with two intersecting sets of fibers to derive analytical nonlinear stress-strain models, this paper

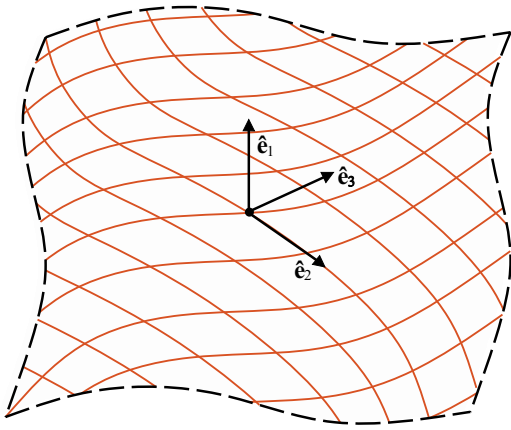


Figure 3. Schematic of a general, fiber-reinforced curved membrane. \mathbf{e}_1 is the surface normal, \mathbf{e}_2 is fixed tangent to one of the fibers, and the other fiber lies between \mathbf{e}_2 and \mathbf{e}_3 .

takes the first step toward extending the modeling of fiber arrays to arbitrary, convex fiber-reinforced surfaces.

A simple approximation of a surface in three-dimensional space is the tangent to a point on that surface. If the tangents do not vary with respect to the point chosen, the surface is a planar sheet. Expressions for fiber reorientation and associated stiffness variations were derived for this case in Krieg and Mohseni's work. Adding the next level of complexity, a single second-order term, or curvature, can be added to the approximation while maintaining constant parallel tangent lines perpendicular to the plane of principal curvature, forming a cylinder. The introduction of an additional second-order term gives the curvature in both principal directions on a surface to form a general, three-dimensional curved surface.

In this section, we establish techniques for modeling the fiber reorientation on a convex curved surface using generalized curvilinear coordinates and focusing on the reorientation of these components with respect to the constant magnitude of a differential fiber length. We then present this technique to solve for the canonical cases of a sphere, where both principal curvatures are equal, and compare it to the simpler cases of a circular conical frustum and a planar sheet to show how this modeling would be applied to a variety of geometries.

2.1 General Formulation

First, the nature of the constraint applied by the fibers must be considered. The tensile modulus of the fiber is chosen to be several orders of magnitude greater than that of the elastomer matrix. With such a large difference, the fibers are considered inextensible with all deformation occurring in the elastomer, resulting in significant fiber reorientation. Additionally, the fibers are considered to have a negligible contribution to bending stiffness. These assumptions are established by Krieg and Mohseni (2017) for a planar sheet, and they can be used to establish a mathematical relationship between fiber inextensibility and reorientation. To accomplish this for three dimensional shapes, we first consider the fiber length, which is defined as a curve along the surface of the membrane.

The fiber length can locally be considered a vector on the surface of the elastomer with a constant magnitude

$$L = \int_C |ds|, \quad (1)$$

where the differential fiber length, ds , can be defined in terms of general orthogonal curvilinear coordinates,

$$d\mathbf{s} = \frac{\partial \mathbf{s}}{\partial x_1} dx_1 + \frac{\partial \mathbf{s}}{\partial x_2} dx_2 + \frac{\partial \mathbf{s}}{\partial x_3} dx_3 \quad (2a)$$

$$= h_1 dx_1 \mathbf{e}_1 + h_2 dx_2 \mathbf{e}_2 + h_3 dx_3 \mathbf{e}_3, \quad (2b)$$

$$h_i = \left| \frac{\partial \mathbf{s}}{\partial x_i} \right|, \quad (2c)$$

where h_i are the scale factors, dx_i are the components in each base direction, and \mathbf{e}_i are the unit base vectors. This provides a relationship between the components of the differential fiber length. The problem is simplified considerably if a coordinate system is chosen that defines one of the components to be normal to the surface, as the fibers are fixed to the surface and therefore contain no normal component, as shown in Figure 3. This can be seen in Krieg and Mohseni's work, where Cartesian coordinates were used with the z -axis normal to the plane; therefore, there was no fiber component along this axis. In a cylindrical system, the radial component is normal to the tangent plane and fiber components are along the polar and longitudinal axes. A spherical system also accomplishes this if the fibers are completely defined using the polar and azimuthal angles. For more complex systems, a local coordinate system can be used to determine reorientation and then be transformed to a global system.

As stated previously, the constant magnitude of a differential fiber length provides a relation between its components which can be used to determine the reorientation of the fibers. First, the magnitude of the differential fiber length defined in Equation (2) is considered. If we define the first component along the surface normal, we get

$$\frac{dL}{d\gamma} = \sqrt{\left(h_2 \frac{dx_2}{d\gamma}\right)^2 + \left(h_3 \frac{dx_3}{d\gamma}\right)^2}, \quad (3)$$

where $dL = |ds|$ and γ is a general parameter that defines the surface. We next need to define the remaining bases to describe the components of the differential fiber length. By fixing one coordinate direction tangent to one of the fibers, which we will refer to as the fixed fiber, we are able to solve for the movement of the second fiber, which we will refer to as the reorienting fiber, in terms of the first. As the membrane deforms, the fibers restrict deformation along their length, and the membrane is only able to expand through fiber reorientation, which takes place to maximize the planar area encapsulated by the fibers. The differential area between two sets of fibers is

$$dA = |d\mathbf{s}_1 \times d\mathbf{s}_2| \quad (4a)$$

$$= |d\mathbf{s}_1| |d\mathbf{s}_2| \sin \psi, \quad (4b)$$

where the subscripts of ds are used refer to the different fiber sets. dA goes to a maximum when ψ , the angle between the two fibers, goes to $\pi/2$. This is the critical configuration,

where any additional deformation requires fiber extension, as the planar area of the elastomer has already been maximized. Following that the maximum area occurs when the fibers are locally orthogonal and that the surface bases lie tangent to the fibers in this configuration, we next assume that the fibers do not slide past each other. Because of this, the differential length of the fiber with respect to the parameter γ will be constant throughout all stages of deformation and can be solved for from one of the known stages. If the desired configuration is chosen such that the two sets of fibers are locally orthogonal, the expression for differential fiber length with respect to γ simplifies to

$$\frac{dL}{d\gamma} = h_3 \left. \frac{dx_3}{d\gamma} \right|_f, \quad (5)$$

where f refers to the final configuration associated with the critical angle. Then by applying this relationship to the original fiber length equation shown in Equation (3), we get an equation for fiber reorientation at any configuration as

$$\left(h_3 \left. \frac{dx_3}{d\gamma} \right|_f \right)^2 = \left(h_2 \frac{dx_2}{d\gamma} \right)^2 + \left(h_3 \frac{dx_3}{d\gamma} \right)^2, \quad (6a)$$

$$\frac{dx_2}{d\gamma} = \frac{1}{h_2} \left[\left(h_3 \left. \frac{dx_3}{d\gamma} \right|_f \right)^2 - \left(h_3 \frac{dx_3}{d\gamma} \right)^2 \right]^{0.5}, \quad (6b)$$

which relates the two surface components of the fiber and can be used to describe the kinematics of the fiber-reinforced membrane. If the desired configuration is chosen as anything other than an orthogonal fiber mesh, Equations (5) and (6) must simply be modified to account for the additional differential terms.

This technique allows us to describe the kinematics of fiber reorientation that govern the deformation space of the reinforced membrane. For specific geometries, a constraint can often be defined that simplifies the closed-form solution of the model. In Sections 2.2 and 2.3, we illustrate this concept by defining desired membrane geometries that we use as the critical cases of fiber reorientation. To accomplish this, we define an orthogonal mesh of fibers on the desired surface. Deformation of the membrane past this critical configuration would require fiber extension, which is limited by the fibers' high tensile strength. In the following sections, several special cases are presented where the membranes deform from a flat membrane to their final desired configuration.

2.2 Special Case: Sphere

To demonstrate an example of the kinematic modeling described above, we assume a simple case of a system with two equal principal curvatures, which is that of a sphere. As such, we adopt a spherical coordinate system to describe the symmetry associated with this configuration with radius R , polar angle ϕ , and azimuthal angle θ , shown in Figure 4. By applying this to Equation (3), we obtain

$$\frac{dL}{d\gamma} = \sqrt{\left(\rho \frac{d\theta}{d\gamma} \right)^2 + \left(R \frac{d\phi}{d\gamma} \right)^2}, \quad (7)$$

where the polar radius $\rho = R \sin\phi$.

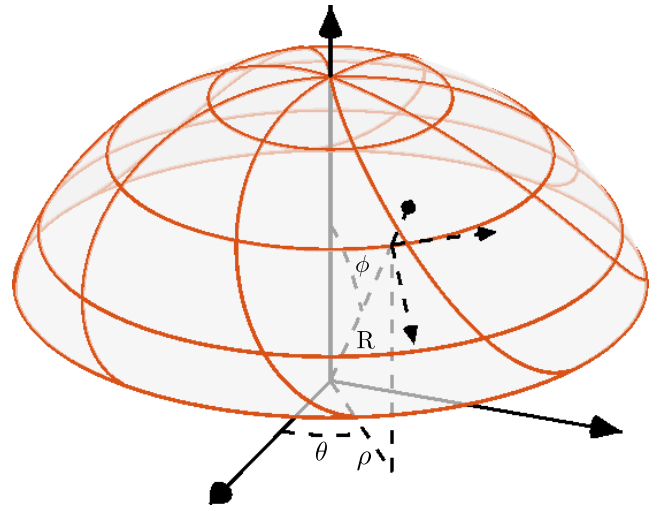


Figure 4. Schematic of the fiber-reinforced spherical membrane at an intermediate stage of inflation. The circular set of fibers that act along the θ direction restrict the polar radius ρ , while the second set of fibers straighten to form major arcs along the ϕ direction, resulting in hemispherical geometry at full inflation. The origin is set at the center of curvature and not the center of the clamped edges of the circular membrane to keep the radial coordinate normal to the surface.

If we choose to define the desired configuration to be a hemisphere at the critical case of fiber reorientation, we can establish one set of fibers as major arcs along the polar angle ϕ . To complete the fiber mesh, a set of fibers needs to be applied in the orthogonal direction, which form rings along the azimuthal angle θ . This layout can be seen in an intermediate stage of inflation in Figure 4. We want the hemisphere to be formed by inflation of a flat circular membrane. This leads us to orient the fiber circles along the θ direction to be concentric with the outer edge of the clamped membrane, making the rings have constant polar radii through all stages of deformation. This makes ρ a convenient parameter to describe the geometry, so we set $\gamma = \rho$. Additionally, while transitioning between the flat plate, which can be treated as a spherical cap with an infinite radius, and the hemisphere, we assume that the membrane maintains the geometry of a spherical cap at every point of inflation. This allows for a kinematic description of the membrane's geometry to be established without requiring knowledge of the stresses experienced by the membrane. Justification for this approximation can be found in Appendix A. We can then characterize the polar angle ϕ and its spatial derivative as

$$\phi = \sin^{-1} \left(\frac{\rho}{R} \right), \quad (8a)$$

$$\frac{d\phi}{d\rho} = \frac{1}{R \cdot \sqrt{1 - \left(\frac{\rho}{R} \right)^2}}. \quad (8b)$$

As shown in Equation (5), the magnitude of the differential fiber length with respect to the parameter γ can be defined by its final configuration. This corresponds to when the fibers form major arcs along the ϕ direction. Presenting this mathematically, we obtain

$$\frac{dL}{d\rho} = R \left. \frac{d\phi}{d\rho} \right|_f = \frac{1}{\sqrt{1 - \left(\frac{\rho}{R} \right)^2}}, \quad (9)$$

where a is the inner radius of the membrane clamp ring (shown in Figure 12), which is the radius of the final hemisphere, R .

Finally, the unknown component of the reorienting fiber can be solved for by applying the relations established in Equations (8b) and (9) to Equation (7) and rearranging the expression to give

$$\frac{d\theta}{d\rho} = \frac{\sqrt{\frac{1}{1-\left(\frac{\rho}{a}\right)^2} - \frac{1}{1-\left(\frac{\rho}{R}\right)^2}}}{\rho}. \quad (10)$$

Then, solving for θ as a function of parameter ρ simply requires integration,

$$\theta = \theta_0 + \frac{a}{\rho} \sqrt{1 - \left(\frac{\rho}{a}\right)^2} \sqrt{1 - \left(\frac{\rho}{R}\right)^2} + \sqrt{\frac{1}{1 - \left(\frac{\rho}{a}\right)^2} - \frac{1}{1 - \left(\frac{\rho}{R}\right)^2}} F\left(\sin^{-1}\left(\frac{\rho}{a}\right), \left(\frac{a}{R}\right)^2\right) \quad (11)$$

where $F(\psi, m)$ is the incomplete elliptical integral of the first kind, see [Abramowitz and Stegun \(1972\)](#).

As the membrane is treated as a spherical cap, we can solve for the radius R used in Equation (11) from the volume

$$V = \frac{1}{3}\pi \left(R - \sqrt{R^2 - a^2}\right)^2 \left(2R + \sqrt{R^2 - a^2}\right). \quad (12)$$

V ranges from 0 in the planar configuration to the critical volume of the inflated membrane, which can be determined by setting the radius of curvature to a

$$V = \frac{2}{3}\pi a^3. \quad (13)$$

Once the radius R is determined with Equation (12) and used to solve for θ (Equation (11)) and ϕ (Equation (8a)), the above analysis provides the spatial configurations of the fibers at all inflation levels, which can be used to determine the configuration needed to fabricate a flat membrane.

2.3 Special Case: Conical Frustum

In addition to the spherical membrane, a membrane which deforms to a conical frustum from a flat plate has also been designed to demonstrate the versatility of the proposed model. The modeling for this new geometry progresses in a similar fashion to that of the spherical membrane, so the first steps are the adoption of an appropriate basis and the definition of the differential fiber length. For a circular conical frustum, cylindrical coordinates provide a convenient coordinate system (Figure 5); however, unlike the case of the spherical membrane, the fibers can have components in all three coordinate directions. To limit the final, critical case, circular rings along the θ direction, similar to the spherical membrane, are used in conjunction with radial fibers which form the conical surface. As such, the expression for the differential fiber length of the reorienting fibers is

$$\frac{dL}{d\rho} = \sqrt{1 + \left(\rho \frac{d\theta}{d\rho}\right)^2 + \left(\frac{dz}{d\rho}\right)^2}. \quad (14)$$

Similar to the approach taken in the spherical case where an approximation of the geometry during intermediate stages

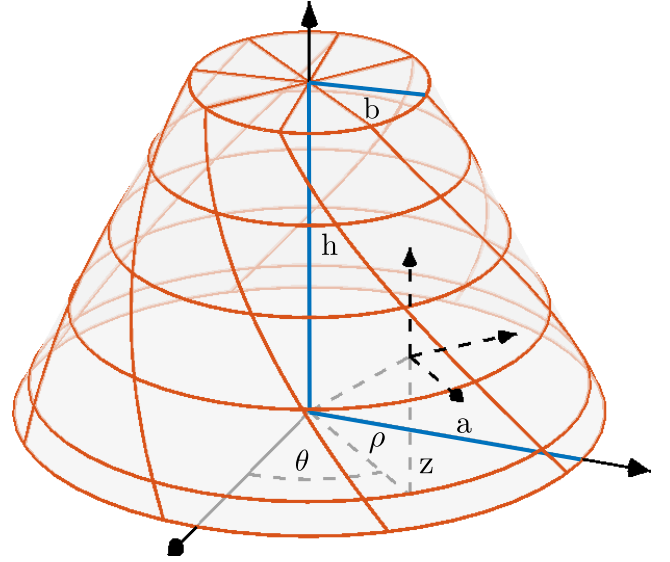


Figure 5. Schematic of the geometry of a conical frustum at an intermediate stage of inflation. The circular set of fibers that act along the θ direction restrict the radius ρ , while the second set of fibers straighten to form the sides of the conical frustum. The conical frustum's height, h , base radius, a , and top radius, b , are also shown.

assumed a spherical cap, an approximation of the conical frustum provides information on the fiber reorientation in the conical case. As the membrane forms a circular conical frustum in both the initial planar and final critical configurations, the membrane is approximated to maintain this shape through every stage of inflation. From this geometry, the differential component of the fiber length along the longitudinal axis can be defined as

$$z = \frac{h}{a-b} (a - \rho), \quad (15a)$$

$$\frac{dz}{d\rho} = \frac{-h}{a-b}, \quad (15b)$$

where a is the inner radius of the membrane clamp ring and b is the radius of the innermost ring along the angle θ , as shown in Figure 5. From the desired final configuration, we know that there is no component of the radial fiber acting along the θ direction; therefore, the differential fiber length with respect to ρ through all stages of inflation can be defined as

$$\frac{dL}{d\rho} = \frac{dz}{d\rho} \Big|_f = \sqrt{1 + \frac{h_f}{b-a}}, \quad (16)$$

where h_f is the height in the final configuration. By combining Equations (15b) and (16) and solving for the unknown fiber component,

$$\frac{d\theta}{d\rho} = \frac{1}{\rho} \sqrt{\frac{h_f^2 - h^2}{(a-b)^2}}, \quad (17)$$

$$\theta = \theta_0 + \sqrt{\frac{h_f^2 - h^2}{(a-b)^2}} \ln \rho, \quad (18)$$

we have the last coordinate needed to describe the fiber position during every level of inflation. This includes the initial configuration, which is solved by setting $h = 0$ and is used to determine the layup used in Section 3.

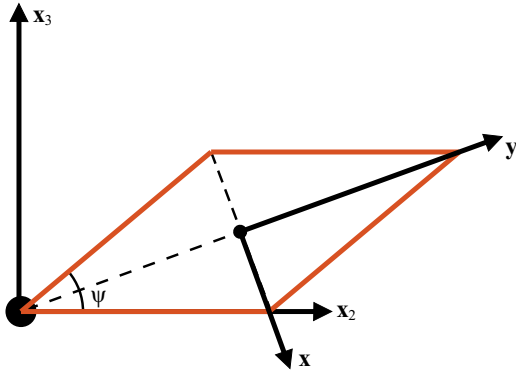


Figure 6. Schematic of a differential fiber element in a planar sheet with a fiber angle denoted by ψ . Fiber lengths are equal to define the x - y coordinate system, but due to the equivalence of parallelogram elements proven in Section 2.5 of [Krieg and Mohseni \(2017\)](#), this model is valid for any parallelogram with angle ψ .

2.4 Special Case: Planar Sheet

Our previous examples focused on extending the analysis used for planar sheets to arbitrary curved surfaces, but the same techniques used for arbitrary curvatures can be applied to the simplified kinematics of a sheet which maintains its planar geometry when deformed. Besides describing how a flat membrane would deform, modeling for a planar sheet would provide a first order approximation and linearization for a general manifold around a point. As such, we can look into the characteristics of the planar sheet to approximately predict how the material will perform for a curved surface. For this case, Cartesian coordinates are adopted, with scale factors equal to 1, which simplifies Equation (3) to

$$\frac{dL}{d\gamma} = \sqrt{\left(\frac{dx_2}{d\gamma}\right)^2 + \left(\frac{dx_3}{d\gamma}\right)^2} \quad (19)$$

For straight fibers, like those used by [Krieg and Mohseni \(2017\)](#), the differential components of the fiber lengths do not vary in space, and the magnitude of the differential fiber length is purely a function of its planar components. This allows Equation (19) to be simplified and for the global kinematics to be defined by a single quantity ψ , the acute angle between the fibers. Defining \mathbf{e}_2 along the fiber, the components of a differential length of the second fiber become a projection of dL ,

$$dx_2 = dL \cdot \cos\psi, \quad (20a)$$

$$dx_3 = dL \cdot \sin\psi, \quad (20b)$$

where ψ is the angle between the two fibers. This projection reaches a maximum at the critical angle $\pi/2$,

$$dL = dx_3 \Big|_f. \quad (21)$$

By rotating the coordinate system such that the coordinates act between the nodes of the quadrilateral element formed, as shown in Figure 6, we are able to obtain the principal strains in the material. Determining the distance between the nodes of a differential element along the x -axis, we get

$$l_x = \sqrt{(dL - dx_2)^2 + dx_3^2}, \quad (22a)$$

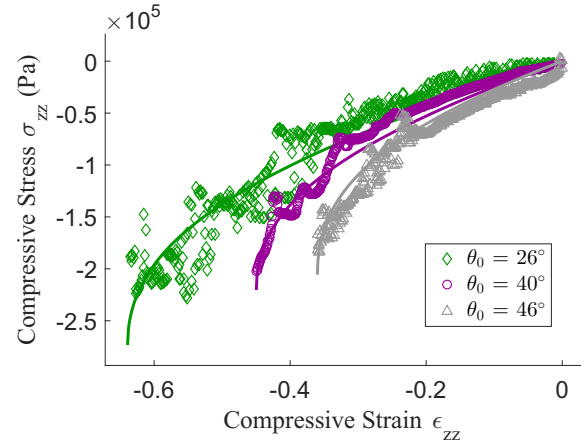


Figure 7. Stress-strain relationship for the soft composite sheets with various initial fiber angles, taken from Figure 11 of [Krieg and Mohseni \(2017\)](#). The solid lines in are calculated from the analytical stress-strain model in [Krieg and Mohseni \(2017\)](#).

$$= \sqrt{dL^2(1 - \cos\psi)^2 + dL^2\sin^2\psi}, \quad (22b)$$

$$= \sqrt{2dL^2(1 - \cos\psi)}. \quad (22c)$$

By a similar process, the distance between the nodes of a differential element along the y -axis can be determined, leading to

$$l_y = \sqrt{2dL^2(1 + \cos\psi)}. \quad (23)$$

Defining the strains as the displacement between the initial and current configurations with respect to the initial configuration, the strains become

$$\epsilon_x = \left[\frac{1 - \cos\psi}{1 - \cos\psi_0} \right]^{0.5} - 1, \quad (24a)$$

$$\epsilon_y = \left[\frac{1 + \cos\psi}{1 + \cos\psi_0} \right]^{0.5} - 1, \quad (24b)$$

where ψ_0 is the initial angle between the fibers. These are the exact kinematic expressions obtained by [Krieg and Mohseni \(2017\)](#), which are then used to determine the nonlinear stress-strain response of the material.

Ultimately, any deformation of these soft structures will be the result of some external loading, such as stresses imposed by soft actuators. As an example, consider a DEA with conductor plates oriented parallel/tangent to the surface, which will create compressive stress in the normal direction resulting in planar expansion. By introducing a term for the total compression of the soft material, which is coupled to the material Poisson ratio, the two planar components of strain were related to the third component of strain in the sheet normal direction ([Krieg and Mohseni 2017](#)), and reinforced sheets were shown experimentally to produce planar expansion in a desired direction up to 14 times that of an unreinforced sheet, matching well with the kinematic model associated with fiber reorientation.

As the sheet is compressed, the fiber angle increases to account for planar expansion, and the elastic modulus of the entire composite structure increases significantly. In order to model the nonlinear stress-strain relationship in fiber-reinforced sheets under large deformations analytically,

Krieg and Mohseni (2017) considered the elastomeric matrix and fiber arrays as independent systems that interact through local stresses in the planar directions to create the constrained deformations. The unreinforced elastomer is an isotropic, homogeneous material, meaning that compressing a sheet of the elastomer results in an outward strain in each of the planar directions as governed by the material's Poisson ratio. When the sheet is reinforced by fiber arrays, the planar strains are instead governed by the fiber orientation, as described previously. The stresses transferred between the fibers and elastomeric matrix in the planar directions can then be calculated as the stresses required to create the reinforced sample strains.

Figure 7 shows the stress-strain relationship for several flat, fiber-reinforced sheets with different initial fiber angles, along with the analytical model for the total stress and strain. The analytical modeling shows excellent agreement with measured stress and strain data, validating the methodology. As a first order approximation, small regions of a general 3D sheet can be considered planar to solve for local stress-strain relationships, assuming that the characteristic size of that region is small compared to the radii of curvature. Then, the local stress-strain relationship can be integrated over the entire surface to get the macroscopic relationship. It should also be noted that there is a significant increase in elastic modulus as the fiber angle approaches the critical value. This stiffening associated with fiber reorientation is important because the structure will be easily deformed while in a resting state, but in the final configuration, fiber reinforced sheets will attain much higher structural stability. In section Sections 4.3 and 4.4, we discuss specific applications of a fiber reinforced sheet that deforms into a hemisphere when pressurized, namely using the device as either a flexible buoyancy bladder or as an appendage interacting with external loading. In both applications, the drastic increase in stiffness at the final configuration aids in the desired application. The increase in stiffness prevents rupture of the buoyancy bladder at increased depths and also helps maintain the desired shape even under significant external loading.

3 Fabrication

Fabrication of the membranes tested in this study was conducted in two main steps: fiber layup (Section 3.1) and two-stage elastomer molding (Section 3.2).

3.1 Fiber Layup

The fiber-reinforcement patterns for the membranes designed for this study were prepared on 3D-printed molds (3D Systems ProJet MJP 2500 Plus). The mold designed for the spherical final configuration is shown in Figure 8. Extruded posts trace the path of each fiber, whose orientation was determined based on the modeling in Section 2. The maximum fiber density is determined by the ability to lay out these posts without them crossing the path of another fiber. Small extrusions jut out from each post to raise the fiber off the base of the mold, ensuring that elastomer will encase as much of the fiber as possible during the molding process. If the fibers make contact with the base of the mold, it is likely that they will delaminate while removing the membrane

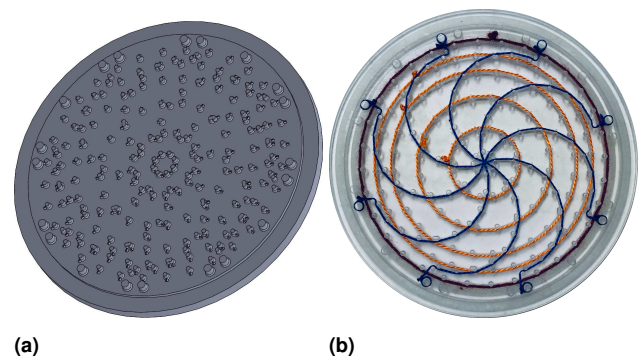


Figure 8. CAD model of membrane mold base for spherical-configuration fiber layup (a) and completed fiber-reinforcement mesh (b). The outermost circular fiber is included to provide extra stiffness in the completed membrane at the clamping surface.

from the mold, ruining the sample in the process. The larger posts on the outer edge result in holes for clamping screws and serve as an anchor point for each of the radial fibers.

Cotton fibers were chosen to enhance bonding with an elastomer matrix. Ecoflex 30 elastomer (Smooth-On, Inc.) was chosen as the matrix of the composite due to its combination of large strain at rupture (allowing for large deformations) and stiffness (to prevent issues with clamping). The fibers are arranged as seen in Figure 8, with circular fibers shown in orange and radial fibers shown in blue. An additional, outermost circular fiber lies under the clamp to provide extra, more uniform stiffness for a proper seal with the clamp base (see Section 4.1 and Figure 8).

While the radial fibers have anchor points to aid in the layup process, the circular fibers do not have anything to hold them in place. Therefore, they are laid down first so the radial fibers can hold them in place once the layup is completed. Each circular fiber was pre-tied with a simple noose knot before being placed on the mold base (Figure 9b) and tightened around its respective guide posts. The two ends of the fiber were then tied with a square knot before being trimmed as short as possible. Finally, the knot was coated with a cyanoacrylate glue (Loctite Ultrageel Control) to prevent untying at high membrane stresses (Figure 9c).

Looming the radial fibers is significantly less difficult than looming the circular fibers. For each fiber, a knot was tied around the anchor at one end of a fiber profile (Figure 9e). While maintaining tension in the fiber, the fiber was pulled around the proper guide posts before tying the same knot on the opposite anchor point (Figure 9f). Care was taken to ensure that the fiber was fully extended before tying the final knot and trimming loose ends (Figure 9g).

The fiber-layup method presented here differs from previous work which has utilized various methods for laying up fibers, such as molded cavities for fiber alignment (Galloway, Polygerinos, Walsh and Wood 2013), rubber cement for fiber adhesion (Bishop-Moser, Krishnan, Kim and Kota 2012), linear fiber layups on elastomeric tapes (Huang, Lu, Zhu, Clarke and Suo 2012), embroidered fibers with soluble supports (Ceron, Cohen, Shepherd, Pikul and Harnett 2018), or loomed fibers encased in injection molded elastomer (Krieg and Mohseni 2017), in that it provides a rigid support structure for laying arbitrary, planar, curved

fiber patterns. Existing processes do not provide a stable base for tensioning planar, curved fibers in soft elastomers while sufficiently preventing deviation from the desired curve, which is necessary for the samples in this paper. Without this tension to ensure that the cotton fibers are taut, the fibers could potentially retain some extensibility, which invalidates the fiber inextensibility assumption made in Section 2.

3.2 Two-Stage Molding Process

Molding of the fiber-reinforced membranes took place in two stages. For each stage, the Ecoflex 30 elastomer was thoroughly mixed and degassed in a vacuum chamber before being poured. Each mold was also sprayed with Universal Mold Release (Smooth-On, Inc.) to aid in removing the membrane from the mold. The first stage embedded the completed fiber layup (Figure 9h) in elastomer. After pouring the elastomer over the fibers, the mold (Figure 10) was placed back into the vacuum chamber to pull elastomer between the cotton threads of the fibers. This helped to ensure proper bonding between the elastomer and the fibers. After degassing, a thick acrylic disk was placed over the open surface of the mold, the mold and disk were flipped upside down to allow any residual bubbles to rise to the surface that is filled in stage 2, and a weight was placed on top while the elastomer cured.

The second stage started with the output of the first stage and the stage 2 mold, both shown in Figure 10. The pattern seen on the surface of the half-completed membrane is the negative of the guide posts, anchor points, and clamp holes. This molding stage brought the membrane to its final thickness and filled in all of the cavities left by the guide posts while leaving holes for the clamp screws and anchor points. After placing the first half of the membrane into the stage 2 mold, cleaning the surface of the sample with rubbing alcohol, and pouring elastomer in, the sample was again placed in the vacuum chamber to ensure that any significant air pockets remaining in the fibers and the guide post negatives were removed. Once degassing was complete, another acrylic disk was placed over the open side of the mold, a weight was placed on top, and the sample was allowed to cure. The unreinforced membrane was fabricated by completely filling the stage 2 mold without completing stage 1. Once complete, the membranes measured 114 mm in diameter and 5 mm in thickness. After inflation to the critical case, the spherical and conical membranes will reach heights of 4.7 cm and 7.0 cm, respectively.

It is important to note that the bonding surface between the stage 1 and 2 molds was designed to be parallel to the direction of maximum strain during inflation. It also includes many small elastomer protrusions that fill the guide post negatives after the second molding stage. These features prevent separation of the two layers at high strains, even with the use of the mold release during the molding process.

4 Experimental Setup and Procedure

In this section, we provide an overview of our inflation experiment setup and procedure in Section 4.1 and describe our data processing techniques for the inflation experiment in Section 4.2. We then describe the external and internal

loading tests in Section 4.3 and explain our practical testing of the membrane in a bioinspired AUV in Section 4.4.

4.1 Inflation Experiment

To validate our model, both the inflated volume of the membrane and the fiber orientation were measured at various stages of inflation. To accomplish this, the sample being tested, whether reinforced with fibers or not, was connected to a facility compressed air line with a simple, mechanical pressure regulator. As the applied pressure was increased by adjusting the regulator, a 20 kPa to 250 kPa absolute pressure sensor (MPXHZ6250AC6T1, Freescale Semiconductor) sampled by a 16-bit ADC (MAX1167BEEE+, Maxim Integrated Products) controlled by an Arduino Mega 2560 provided an average value for the pressure over a 1 second interval. While the pressure was averaged, pictures were taken of the membrane from the front (to show the fiber pattern) and side (to calculate volume) using 8 MP digital cameras (Figure 11).

The membrane was fixed to our setup for pressure testing using the clamping assembly shown in Figure 12. A quick connect tube fitting for 8 mm tube was threaded into a 0.25 in thick laser-cut (ULS PLS6MW, 50 W CO₂ laser) delrin base. Blind holes were drilled into the base for dowel pins, which were placed at the end of each fiber to prevent the fiber from pulling the membrane out of the clamp. This also ensured that the fibers maintained the correct orientation during clamping and testing. A 3.2 mm thick ring with an inner diameter of 9.37 cm was used to clamp down on the edge of the membrane. Helicoil inserts in the base mated to twelve 4-40 screws to ensure a strong and even clamping force.

4.2 Image Processing

Both the volume and fiber orientation measurements required simple image processing using color thresholding to complete. Volume analysis for both reinforced and unreinforced samples is described first, followed by the determination of the fiber orientation.

Volume Analysis: Matlab was used for image analysis to determine the volume of the inflated membrane at each pressure step. Images from the experiments were taken and altered for ease of processing using GIMP. The known diameter of the clamp was used as a reference length and is denoted by the green rectangles in Figure 13. In images where the largest diameter of the membrane was equal to the interior diameter of the clamp, the volume of the inflated membrane was calculated as a spherical cap,

$$V_{\text{spherical cap}} = \frac{1}{6}\pi h(3a^2 + h^2), \quad (25)$$

where a is the inner radius of the clamp and h is the height of the membrane (see Figure 13).

The unreinforced membrane expanded to a spheroidal profile in some images, necessitating a slightly different volume calculation:

$$V_{\text{spheroid}} = \frac{4}{3}\pi\alpha^2\beta_1, \quad (26)$$

where α is the semi major axis (measured using the blue rectangle) and β_1 is the semi minor axis, minus a spheroidal

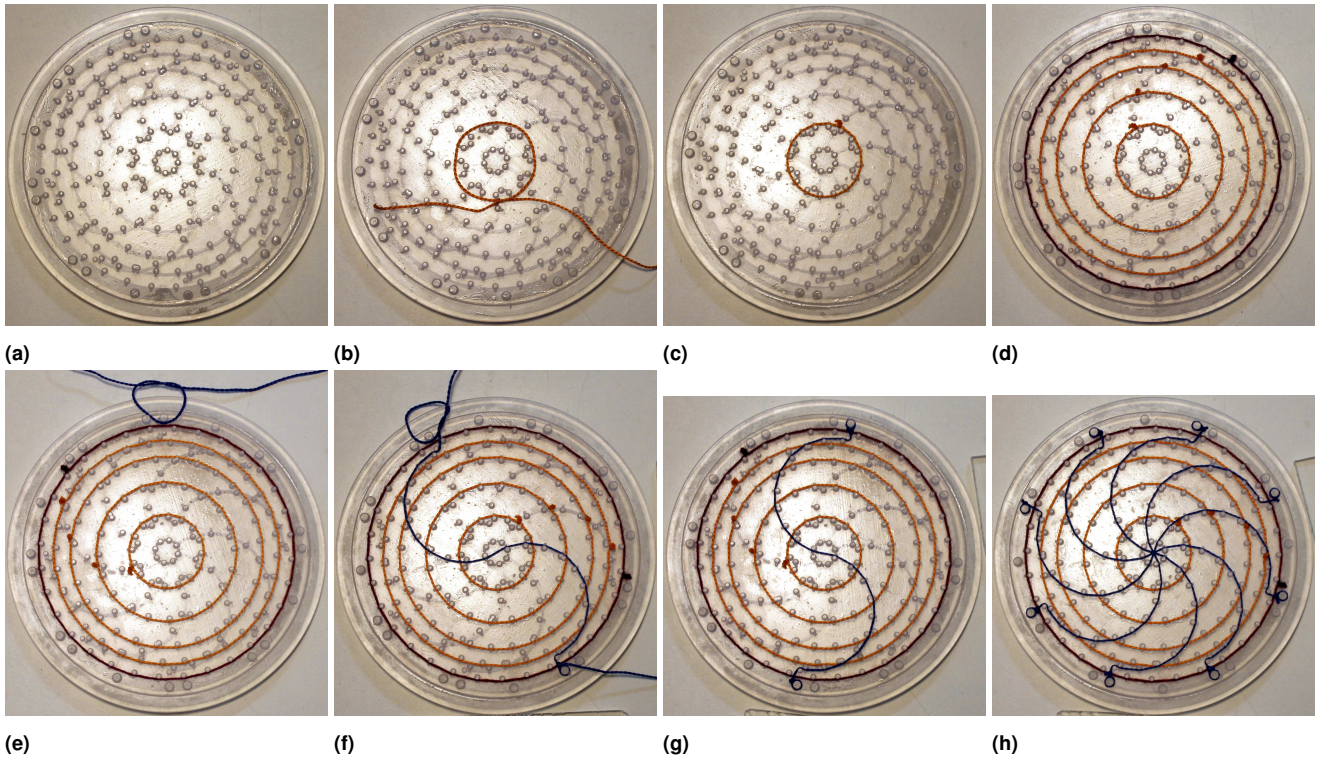


Figure 9. Step-by-step fiber layout. The fiber pattern is traced by extruded guide posts on a 3D printed mold shown in (a). Circular fibers are placed around their respective guide posts (b), tightened, trimmed, and glued (c), resulting in 5 total circular fibers to restrict radial deformation (d). Radial fibers are tied to an anchor point (e), routed around their guide posts (f), tightened, and trimmed (g). This completes the fiber layout with 5 circular fibers and 4 radial fibers to restrict the final radius of curvature of the membrane (h).

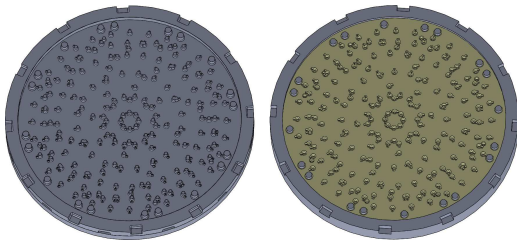


Figure 10. Stage 1 mold with height offset ring installed (left) and stage 2 mold with the output of the stage 1 mold inserted (right). At the beginning of stage 2, the surface of the membrane is covered with holes from the guide posts in the stage 1 mold. These are filled in the stage 2 molding process. Fibers are not shown in this image.

cap

$$V_{\text{spheroidal cap}} = \pi\alpha^2 \frac{h^2(3\beta_1 - h)}{3\beta_1^2}, \quad (27)$$

where h is the height of the spheroidal cap (see Figure 13).

The image-based volume analysis was validated by measuring the mass of water pumped into the membrane at various pressures. This additional experiment confirmed that lens distortion did not introduce significant errors into the volume analysis.

Fiber Orientation Comparison: Image analysis for the fiber orientation comparison was performed using a combination of GIMP and Matlab. After correcting for lens distortion using the circular fibers (which remain a constant diameter during the experiment) as a reference, a fiber from each image was traced to allow for easier color thresholding.

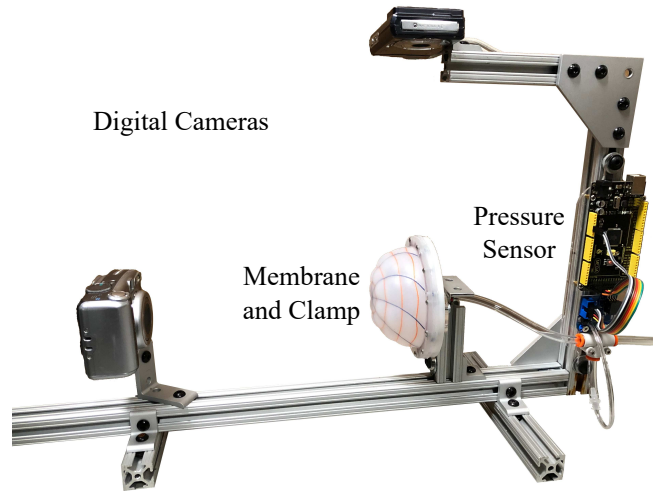


Figure 11. Experimental setup for membrane inflation tests. The membrane was connected to a compressed air source and subjected to various pressures. An Arduino averaged data from a pressure sensor to provide pressure feedback. Two digital cameras, one above the membrane and another in front of the membrane, captured images of the membrane at each pressure step.

Tracing the fibers allows for the angle, θ , of the fiber in each experimental image to be determined as a function of ρ . This function can then be directly compared to the theoretical fiber pattern using the experimental membrane's volume as the input to the model. To obtain a metric for comparison, the

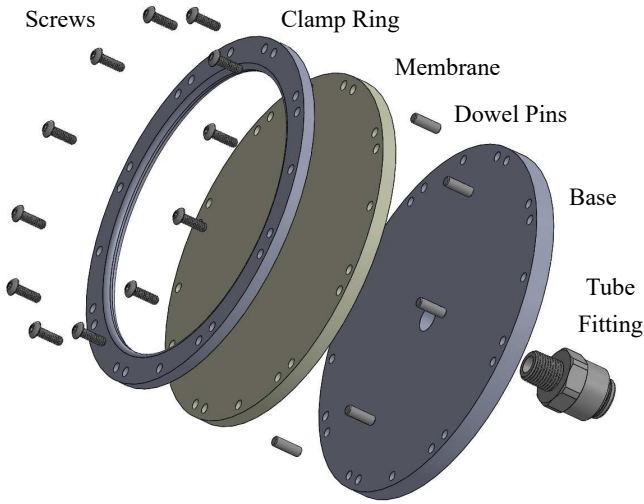


Figure 12. Exploded view of membrane clamping assembly. Compressed air can be released under the membrane to inflate it once it is clamped down. Twelve screws and a clamp ring provide an even clamping force on the membrane. Stainless steel dowel pins provide anchor points for the radial fibers and help to align the membrane on the clamp base.

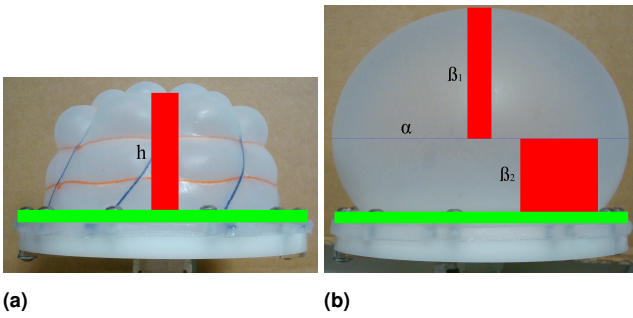


Figure 13. Images prepared for computer volume analysis. The horizontal, green rectangles were superimposed on the clamp, which has a known diameter and was used as a length reference. In (a), the overall shape of the fibers maintained a spherical profile, so the volume of the inflated membrane was calculated as a spherical cap using the vertical, red rectangle as the height of the cap (labeled h). In images where the elastomer expanded between the fiber array, the vertical, red rectangle was drawn to the top of the fiber pattern, as shown here. When the unreinforced control sample reached a spheroidal profile due to its higher strain (b), the volume was calculated as an oblate spheroid minus a spheroidal cap. The pixel-tall blue rectangle was used to measure the major axis of the ellipsoid (α), and the two red rectangles were used to measure the minor axis (β_1) and height of the spheroidal cap ($h = \beta_1 - \beta_2$).

coefficient of determination for the spatial variation between the fiber patterns was established as follows:

$$\bar{\theta} = \frac{1}{n} \sum_{i=1}^n \theta_i, \quad (28a)$$

$$SS_t = \sum_{i=1}^n (\rho_i \cdot \theta_i - \rho_i \cdot \bar{\theta})^2, \quad (28b)$$

$$SS_r = \sum_{i=1}^n (\rho_i \cdot \theta_i - \rho_i \cdot \Theta_i)^2, \quad (28c)$$

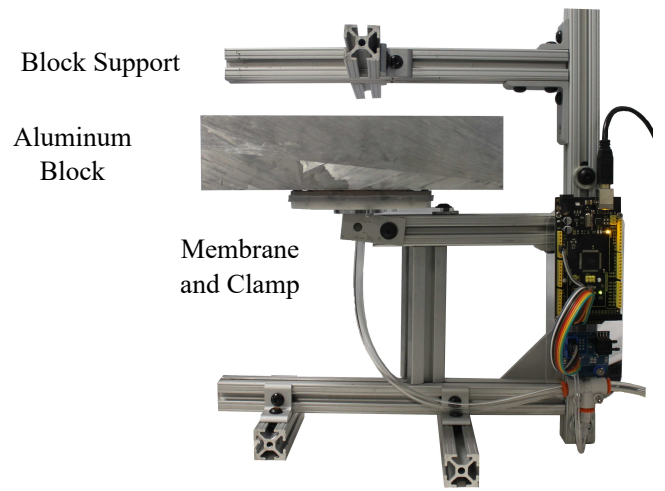


Figure 14. Test setup for external loading test. A 5.84 kg block was lifted up to a brace by the test sample. The inflation pressure was recorded while a photo was taken to show the differences in loaded geometry.

$$R^2 = 1 - \frac{SS_r}{SS_t}, \quad (28d)$$

where θ_i is the measured azimuthal angle at ρ_i , Θ_i is the theoretical azimuthal angle from Equation (11) evaluated at ρ_i , SS_r is the residual sum of squares, and SS_t is the total sum of squares. In addition to the coefficient of determination, the mean absolute error (in degrees) is also calculated

$$MAE = \frac{1}{n} \sum_{i=1}^n |\theta_i - \Theta_i| \quad (29)$$

4.3 Load Experiment

While the inflation test proves our ability to alter the deformation space of the elastomer membrane, it does not reveal how the membrane will behave when placed under a load. This load could come from an external force or from the fluid used to inflate the membrane. Here, we seek to determine the behavior of both the unreinforced and spherical fiber-reinforced membranes under both of these loads.

External Loading: An external load was exerted on the inflated membrane perpendicular to the clamp base by a 5.84 kg aluminum block, shown in Figure 14. The membrane was inflated to the point where it pushed the block against a stabilizing fixture. The internal pressure of the membrane at this point was recorded and a picture was taken for analysis. Both membranes were also inflated to the same hemispherical shape before being loaded by the same aluminum block to directly compare their shape change.

Internal Loading: An internal load was exerted on the membrane tangent to the clamp base by inflating the membrane with water. Images were taken at various pressures to compare the loaded membranes' geometry.

4.4 Buoyancy Experiment

To demonstrate this fiber-reinforcement technique's utility in a practical application, we implemented it on our group's

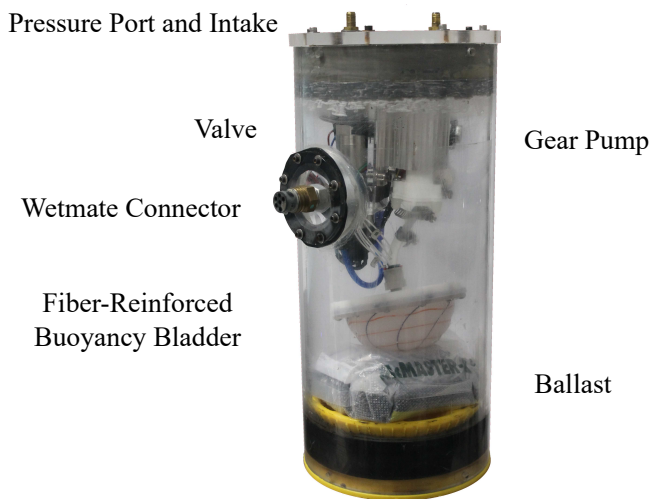


Figure 15. Buoyancy test cylinder with fiber-reinforced membrane as a buoyancy bladder. Pumping water in and out of the bladder changes the density of the device as a whole, causing it to ascend or descend in the water column.

submersible buoyancy test cylinder, shown in Figure 15. Previously, we filled or emptied an inextensible plastic swim bladder with water to change the density of the test cylinder and cause it to ascend or descend in the water column (Sholl and Mohseni 2019). This technique has several disadvantages, including an inability to control the shape of the bladder, which can kink itself or push into other components, and an inability measure the volume of the bladder, which maintains the same pressure as the internal cavity of the test cylinder throughout operation. While the volume of the bladder can be estimated by integrating the flow rate in and out of the bladder or calculating it from the acceleration of the cylinder, such measurements are relatively inaccurate when conducted with small, inexpensive components. If the volume of the bladder is unknown, so is the applied control force resulting from the mass of water inside the bladder. Using the fiber-reinforced membrane instead of an inextensible plastic bladder addresses both of these issues by providing a predictable volume for a given pressure differential and ensuring a more predictable geometry of the bladder at different orientations and volumes. Additionally, fiber reinforcement helps to prevent rupture in the membrane, which could occur more easily in an unreinforced membrane. We plan to integrate the fiber-reinforced buoyancy bladder into our bioinspired AUVs, the CephaloBot (Krieg, Klein, Hodgkinson and Mohseni 2011) and daughter vehicle (Song, Mazzola, Schwartz, Finlaw, Chen, Krieg and Mohseni 2016).

For this test, the buoyancy test cylinder inflated the fiber-reinforced membrane with ambient pool water using a gear pump (Greylor PQ-12DC) to a maximum mass of 0.14 kg. The controller (Sholl and Mohseni 2019) utilized a 100 kPa differential pressure sensor (Freescale Semiconductor MPX5100DP) to determine the membrane's inflation pressure. A 3D-printed attachment for a 25 kPa differential pressure sensor (Freescale Semiconductor MPXV7025DP) was used to monitor the flow rate in and out of the membrane. Depth was measured using a 1 atm gage pressure sensor (Honeywell FP2000).

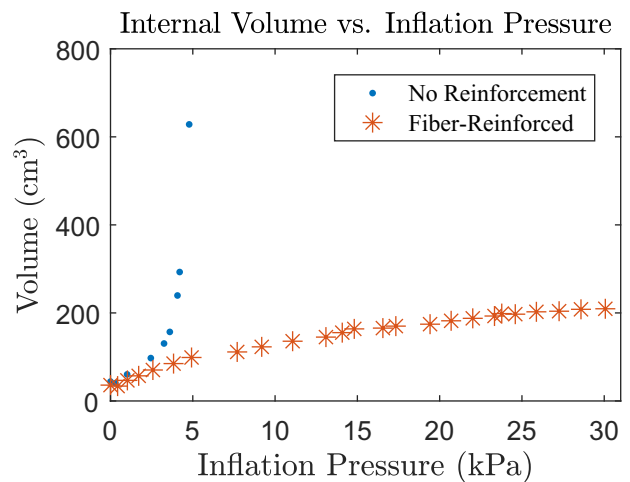


Figure 16. Membrane internal volume as a function of applied inflation pressure for an unreinforced membrane and a spherical, fiber-reinforced membrane. The fiber-reinforced sample appears to reach an asymptote corresponding to the maximum theoretical volume of 215.1 cm³ as the pressure increases, while the unreinforced membrane expands exponentially at low pressures.

5 Results

Here we present the results of our inflation experiment in Section 5.1 and use them to validate our mathematical model in Section 5.2. We also show the deformations of the spherical membrane produced by external and internal loading in Section 5.3 and the performance of our buoyancy test cylinder using a spherical fiber-reinforced bladder in Section 5.4.

5.1 Inflation Experiment Results

The inflated volume of each membrane is shown as a function of pressure in Figure 16. While the spherical fiber-reinforced membrane appeared to reach an asymptote corresponding to the critical volume of 215.1 cm³ by its maximum inflation at 30.10 kPa, the conical fiber-reinforced membrane could only reach 81.8% of its theoretical maximum volume of 254.1 cm³ before the fibers ripped the elastomer matrix at 42.69 kPa, and the unreinforced membrane expanded exponentially at as little as 4.78 kPa.

Figure 17 shows both the unreinforced and fiber-reinforced membranes at various stages of inflation. As expected, the radial fibers straightened throughout the inflation process for both fiber-reinforced membranes. While the circular fibers in both samples successfully prevented radial expansion, the membranes did not reach their fiber-imposed volume limits due to the stiffness of the elastomer, resulting in the curved portions of fiber at maximum inflation, especially in the conical case.

5.2 Comparison with Model

The error between the theoretically-calculated and experimentally-observed fiber patterns can be found in Table 1 and Figure 18. With the exception of the last, near-critical-volume test case of the spherical membrane, the model and experiment show good agreement with an average

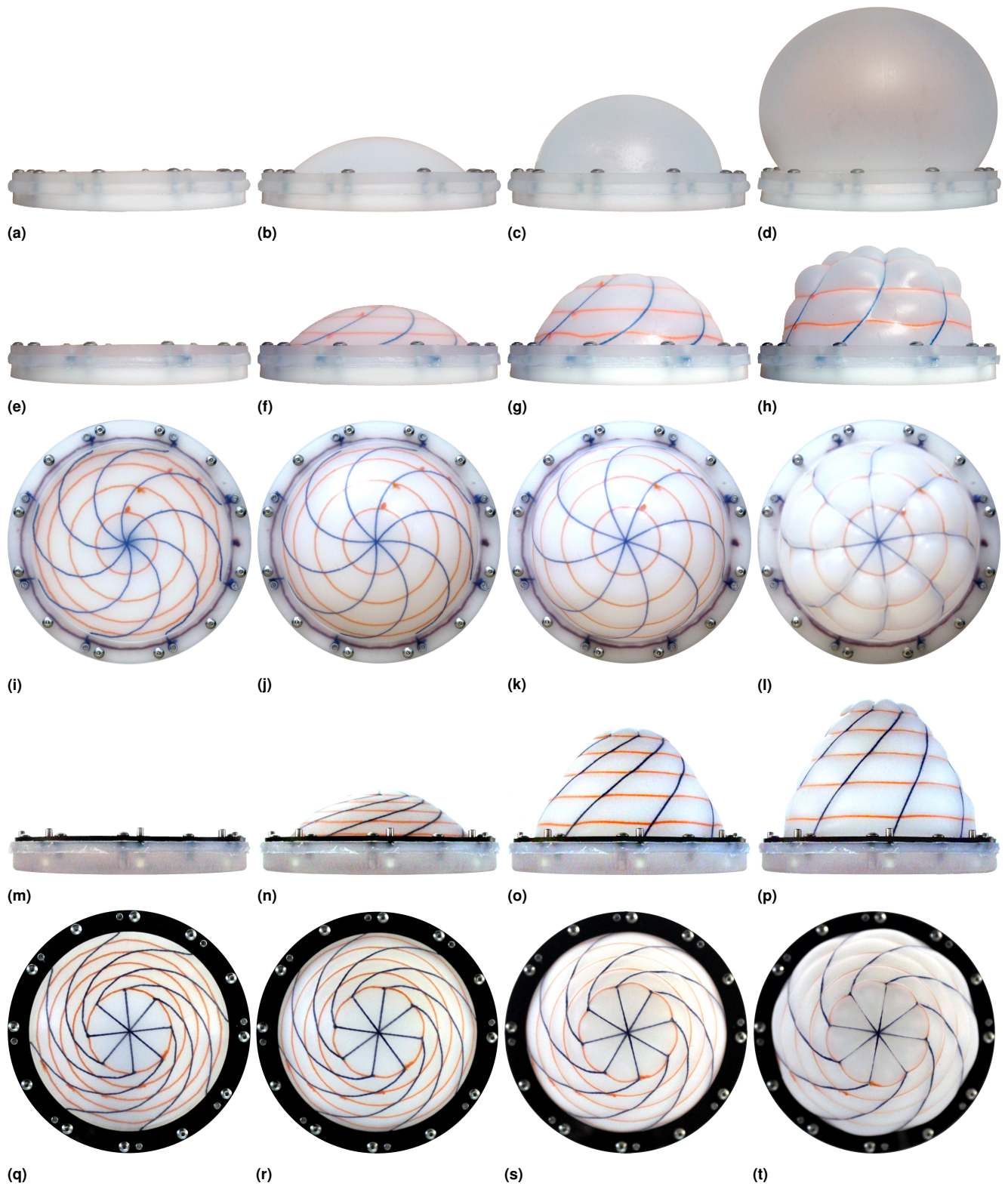


Figure 17. Unreinforced and fiber-reinforced membranes at various stages of the inflation test. A side view of the unreinforced membrane is shown in (a)-(d), a side view of the fiber-reinforced spherical membrane is shown in (e)-(h), a front view of the spherical fiber-reinforced membrane is shown in (i)-(l), a side view of the conical fiber-reinforced membrane is shown in (m)-(p), and a front view of the conical fiber-reinforced membrane is shown in (q)-(t). The internal pressure is increased from 0 kPa to a maximum of 4.78 kPa for the unreinforced membrane, 24.60 kPa for the spherical fiber-reinforced membrane, and 42.69 kPa for the conical fiber-reinforced membrane. Note that as the pressure increases, the radial fibers straighten, bringing the membranes closer to their final configurations.

R^2 value of $0.982 (\pm 2.59^\circ)$ for the spherical membrane and $0.995 (\pm 1.56^\circ)$ for the conical membrane.

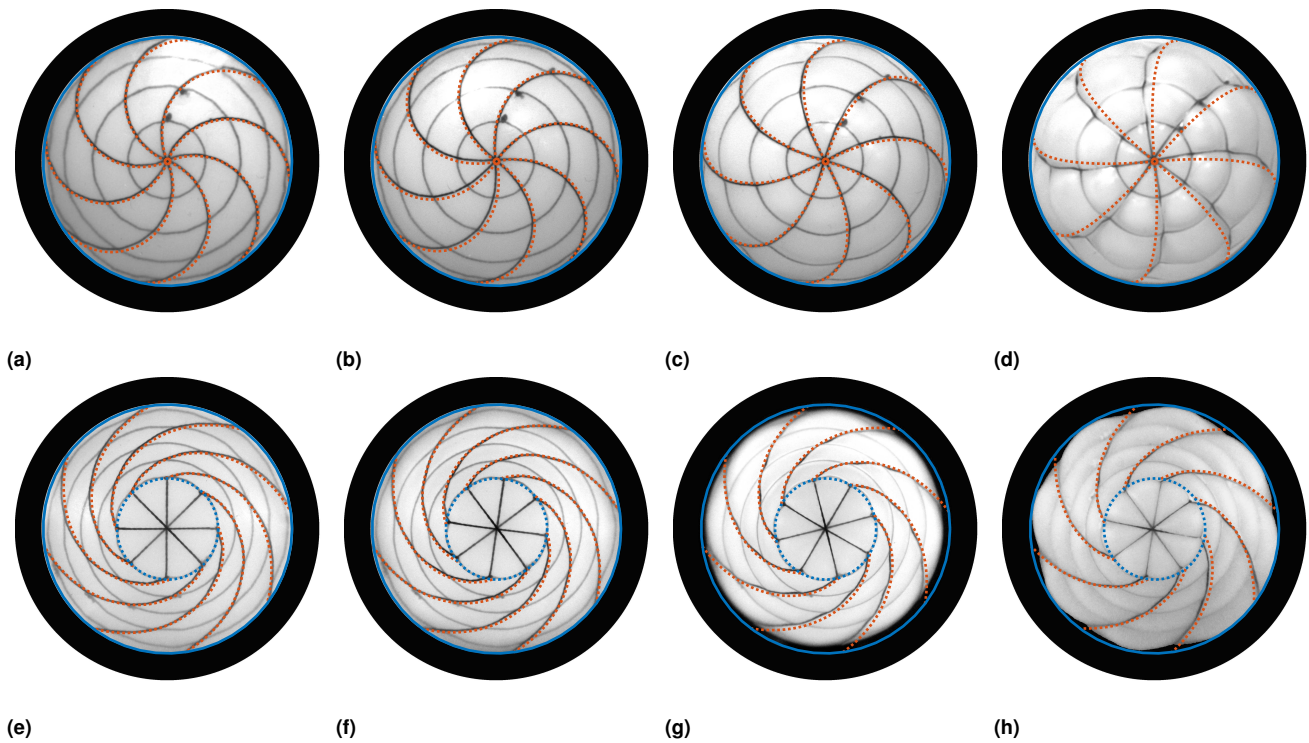


Figure 18. Comparison between modeled and experimental fiber reorientation for the spherical membrane (top) and the conical membrane (bottom). Inflated volume increases for both samples from left to right. The theoretical fiber paths are superimposed upon images of the membranes from the inflation test. Note that the largest errors are in (d), where the spherical membrane approaches its critical volume.

Table 1. Errors between theory and experiment for each of the images shown in Figure 17. The ideal volume is calculated based on the image processing in Section 4.2 and is normalized to the volume of the designed critical case. Pressure data is normalized to the maximum tested pressure, R^2 values are calculated using Equation (28), and MAE is calculated using Equation (29). As the volume of the spherical membrane increases, so does its error, likely due to stress concentrations within the elastomer which prevent the membrane from deforming to the desired shape. The conical membrane exhibits relatively consistent, low errors, further suggesting that the most significant errors only occur near the critical fiber angle, when stress concentrations are highest for the samples presented.

Fiber Pattern	Normalized Ideal Volume	Normalized Pressure	Fiber R^2	Mean Absolute Error
Spherical	16.7%	0.0%	0.998	2.27°
	32.7%	8.6%	0.992	2.35°
	63.1%	36.8%	0.956	3.15°
	91.7%	81.7%	0.670	6.19°
Conical	13.1%	0.0%	0.998	1.35°
	34.5%	20.8%	0.998	1.51°
	66.1%	51.6%	0.991	2.06°
	81.8%	100.0%	0.994	1.33°

5.3 Load Test Results

Here, we report the results of our internal and external load tests on spherical fiber-reinforced and unreinforced membranes.

External Loading: Both the unreinforced and the spherical fiber-reinforced membranes were capable of lifting and

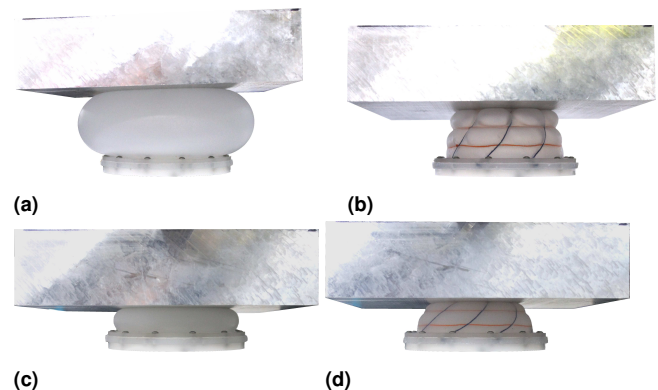


Figure 19. Unreinforced (a,c) and spherical fiber-reinforced (b,d) membranes under a 5.84 kg aluminum block. Note that the reinforced membrane holds its hemispherical shape while the unreinforced membrane is significantly deformed by the weight of the aluminum at both high (a and b) and low (c and d) respective pressures.

supporting the test mass at 11.93 kPa and 31.32 kPa, respectively. As shown in Figures 19a and 19b, the unreinforced membrane was forced to compensate for the lack of sufficient internal pressure by expanding its contact area with the aluminum block to lift it. This need to expand the contact area resulted in the membrane significantly deforming from a hemispherical shape. Due to the higher pressure in the fiber-reinforced membrane, it was able to lift the aluminum block while maintaining a hemispherical geometry.

Figures 19c and 19d show the unreinforced and spherical fiber-reinforced membranes after being inflated to the hemispherical configurations in Figures 17c and 17g,

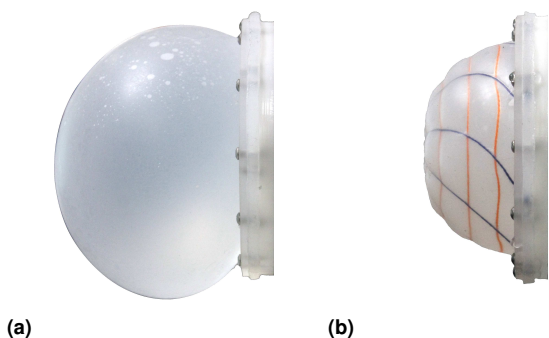


Figure 20. Unreinforced (a) and spherical fiber-reinforced (b) membranes filled with water at 4.42 kPa and 13.17 kPa, respectively. While the unreinforced membrane is capable of holding a larger volume of water, much more precise control over the pressure differential is required to control that volume and the overall geometry of the membrane. To bring the unreinforced membrane in (a) to the same geometry as (b), the pressure only needs to be reduced by 0.82 kPa. The spherical fiber-reinforced membrane, on the other hand, exhibits a larger change in pressure with respect to a change in volume.

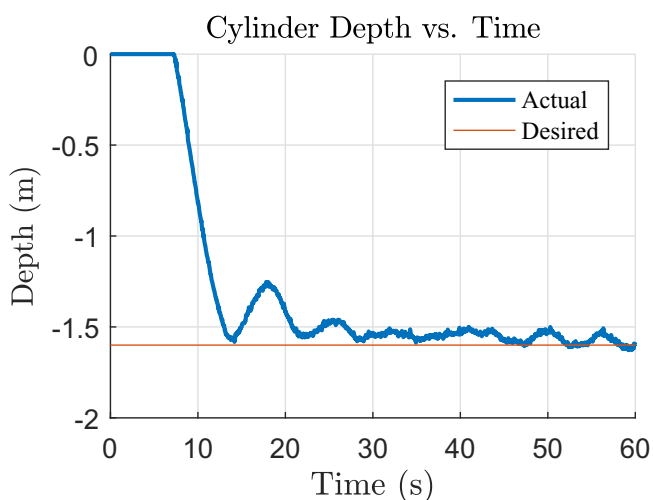


Figure 21. Buoyancy test cylinder performance using a spherical fiber-reinforced membrane as a buoyancy bladder. The mean error past 30 s is 4.4 cm.

respectively, and loaded with the aluminum block. The unreinforced membrane started at 3.29 kPa and increased to 10.99 kPa after loading, whereas the spherical fiber-reinforced membrane increased from 7.61 kPa to 17.82 kPa.

Internal Loading: Images from the internal loading test are shown in Figure 20. The unreinforced membrane can be inflated to a larger volume than the spherical fiber-reinforced membrane, so it was possible to make the membrane deform in the direction of gravity at larger volumes (4.42 kPa in Figure 20a). When filled with water to 3.60 kPa, the unreinforced membrane exhibits nearly identical geometry to the spherical fiber-reinforced membrane at 13.17 kPa in Figure 20b. The spherical fiber-reinforced membrane, on the other hand did not exhibit any observable deformation as a result of the internal load at the maximum possible volume.

5.4 Buoyancy Test Results

The performance of the buoyancy test cylinder fitted with a spherical fiber-reinforced membrane buoyancy bladder is

shown in Figure 21. The cylinder settled to within 10 cm of the depth setpoint of 1.6 m within 20 s of the start of its decent. After the 30 s mark, the system exhibited a mean error of 4.4 cm.

6 Discussion

Figures 16 and 17 strongly suggest that our initial claim to the ability to restrict the deformation space of a soft membrane is valid. The unreinforced membrane's volume exponentially increases at low pressures, making accurate control of the inflated membrane's volume and shape difficult. The fiber-reinforced samples, on the other hand, are clearly restrained to their predefined profiles. While there is elastomer expansion between the fibers at higher pressures (see Figures 17h and 17i), the overall shape and volume of the membranes can still be controlled. Additionally, this expansion between the fibers can be reduced by increasing the fiber density.

The model presented in Section 2 does not consider the stiffness of the elastomer. In the unreinforced case, there is relatively uniform deformation in the membrane as a result of its uniform material properties and loading. However, when fiber reinforcement is introduced, a deformation gradient is developed within the membrane as a result of local reorientation of the fibers. These gradients result in significantly higher required pressures to actuate a fiber-reinforced membrane to a given volume than are required for an unreinforced membrane, as shown in Figure 16.

The differences in the curves shown in Figure 16 speak to the advantages of a fiber-reinforced elastomeric membrane for controls applications. If the membrane is used as a buoyancy bladder in an AUV, as demonstrated in this paper, fiber-reinforcement greatly increases the range of pressures that can be used for volume control over that of the unreinforced membrane. Small changes in the applied pressure in an unreinforced membrane can cause the volume to exponentially increase, which is an issue for small, inaccurate pumps. Since many pumps which meet the performance requirements for an active buoyancy system and the stringent power and space requirements imposed on AUV components are incapable of accurate volume control without other equipment, the ability to control and sense the volume of the buoyancy bladder using pressure alone is a major advantage over non-elastomeric and unreinforced elastomeric bladders.

While the wider pressure range used for inflation of a fiber-reinforced membrane has its advantages, it also makes actuating the membrane to its critical design case without failure of either the membrane or the clamp much more difficult. Due to the geometry of the fiber layups designed for this paper, the elastomer towards the edges of the membrane must deform significantly more than the elastomer in the center of the sample. This results in unmodeled deviations from the predicted fiber pattern close to the critical case (e.g., Figure 18d) and increased stress and deformation at the clamping surface. These stress concentrations lead to failure of the conical membranes before they can approach the critical case, but they can be mitigated in the future either by choosing a softer elastomer matrix or by modeling the

stress-strain relationship within the membrane to design fiber patterns that minimize stress concentrations.

As seen in Table 1, the volume recorded at 0% inflation pressure is 36 cm^3 . This is due to the clamping force that is exerted around the edge of the membrane to maintain a seal against the base. The clamp causes stress concentrations in the elastomer around it, resulting in a slight deformation of the membrane away from the base.

As shown in Figure 21, the buoyancy test cylinder does not initially overshoot the depth setpoint. The controller gains were intentionally tuned for this behavior to avoid hitting the bottom of the testing pool. Also, the error and behavior past 30 s are likely due to custom flow sensor errors at low flow rates and interactions between the buoyancy test cylinder and its tether. Flow sensor errors can be mitigated with further revisions to the sensor geometry, and tether-induced errors will be eliminated once the buoyancy system is employed on the CephaloBot AUV.

While we only present deformation of these soft membranes as a result of increasing the differential pressure across the membrane, many different actuation methods could be utilized. For example, the same effect could be achieved by inducing a stress within the membrane. Such a stress could be created by a dielectric elastomer actuator to generate a pressure differential across the membrane, as we have demonstrated previously in unreinforced elastomers (Sholl, Moss, Kier and Mohseni 2019). This pressure could be used as an adhesive force, as in a suction cup, or to pump fluids. Additionally, the proposed method of fiber reinforcement is not dependent on the fiber material chosen, so long as it is nearly inextensible in the desired range of actuation forces. Enhanced geometric feedback could therefore be provided by replacing the cotton fibers used in this paper with fiber-optic fibers, as used in Galloway, Chen, Templeton, Rife, Godage and Barth (2019).

Since this soft membrane is able to start in a completely flat configuration, stretch to a desired shape, and maintain that shape under a load, it could also be used as an easy-to-pack solution for vehicle airbags. This is especially important for spacecraft applications, where reducing the weight and size of a system can lead to a large reduction in cost.

7 Conclusions

In this paper, we have mathematically shown and experimentally proven that it is possible to design a pattern of fibers that will restrict the deformation of an elastomer membrane to a critical point of expansion. The stiffness of the membrane at that critical point is greatly increased, enabling the soft membrane to both support a load and maintain its shape in the process. Given these characteristics, fiber reinforcement of this kind could provide a technique for more accurately predicting and controlling soft-body deformation.

Future work involves expanding the model for use in more generalized cases. By focusing on the reorientation of a differential element of the fiber, it should be possible to describe the reorientation of a particular fiber configuration on any smooth surface, providing a technique for creating complex three-dimensional soft skins that could be used to control the deformation space of larger soft robotic

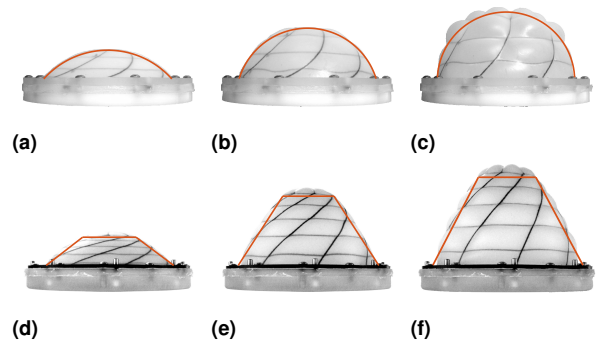


Figure 22. Comparison of the fiber-reinforced membranes to their associated spherical cap and conical frustum geometric assumptions. The approximation of the overall membrane shape at intermediate levels of inflation shows good agreement with the experimental results.

systems. Additionally, the modeling could be expanded to include the stress-strain characteristics of fiber-reinforced membranes, which would allow us to better predict how stress concentrations will influence fiber reorientation in the membrane as it deforms.

A Intermediate Stage Validation

When solving for the reorientation of the fiber-reinforced membranes presented in this paper, an approximation of the membranes' curvature was required to solve for the reorientation of the fibers at intermediate stages of inflation. These intermediate stages were assumed to maintain a spherical cap geometry for the spherical membrane and a conical frustum geometry for the conical membrane.

For the spherical case, the membrane must maintain a spherical cap geometry with an infinite radius of curvature in the initial (planar) case and a radius of curvature equal to the radius of the membrane in the critical (hemispherical) case. Due to the additional fact that the unreinforced membrane maintains a spherical cap profile during inflation up until a hemispherical geometry (Figures 17a to 17c), a spherical cap assumption was made for the spherical fiber-reinforced membrane. We validate this assumption in Figures 22a to 22c. A similar assumption was made in the conical case, where a conical frustum geometry was assumed for the intermediate stages. Overlays of this assumption can be seen in Figures 22d to 22f. Both assumptions exhibit good agreement with the experimental results.

Acknowledgements

This work was partially supported by the Office of Naval Research and the National Science Foundation. The first author was funded by the Department of Defense (DoD) through the National Defense Science & Engineering Graduate Fellowship (NDSEG) Program. The second author was funded by the University of Florida Graduate School Fellowship Program.

References

- Abramowitz M and Stegun IA (1972) *Handbook of Mathematical Functions*. Mineola, NY, USA: Dover Publications. ISBN 978-0486612720.

- Agarwal BD and Broutman LJ (1980) *Analysis and performance of fiber composites*. New York: John Wiley & Sons.
- Anderson EJ and Grosenbaugh MA (2005) Jet flow in steadily swimming adult squid. *Journal of Experimental Biology* 208: 1125–1146. DOI:10.1242/jeb.01507. URL <http://dx.doi.org/10.1242/jeb.01507>.
- Bishop-Moser J, Krishnan G, Kim C and Kota S (2012) Design of soft robotic actuators using fluid-filled fiber-reinforced elastomeric enclosures in parallel combinations. In: *2012 IEEE/RSJ International Conference on Intelligent Robots and Systems*. pp. 4264–4269. DOI:10.1109/IROS.2012.6385966.
- Bolzmaier C, Biggs J and Srinivasan M (2006) Flexible dielectric elastomer actuators for wearable human-machine interfaces. In: *Smart Structures and Materials 2006: Electroactive Polymer Actuators and Devices (EAPAD)*, volume 6168. International Society for Optics and Photonics, p. 616804.
- Bone Q, Pulsford A and Chubb AD (1981) Squid mantle muscle. *Journal of the Marine Biological Association of the United Kingdom* 61(2): 327–342. DOI:10.1017/S0025315400046981. URL <http://dx.doi.org/10.1017/S0025315400046981>.
- Cacucciolo V, Renda F, Poccia E, Laschi C and Cianchetti M (2016) Modelling the nonlinear response of fibre-reinforced bending fluidic actuators. *Smart Materials and Structures* 25(10): 105020.
- Cappello L, Galloway KC, Sanan S, Wagner DA, Granberry R, Engelhardt S, Haufe FL, Peisner JD and Walsh CJ (2018) Exploiting textile mechanical anisotropy for fabric-based pneumatic actuators. *Soft Robotics* 5(5): 662–674. DOI:10.1089/soro.2017.0076. URL <https://doi.org/10.1089/soro.2017.0076>. PMID: 30024312.
- Ceron S, Cohen I, Shepherd R, Pikul J and Harnett C (2018) Fiber embroidery of self-sensing soft actuators. *Biomimetics* 3(3): 24. DOI:10.3390/biomimetics3030024. URL <http://dx.doi.org/10.3390/biomimetics3030024>.
- Clark SK (1987) Composite theory applied to elastomers. Technical Report CR-180322, N87-27035, NASA.
- Fang Y, Pence TJ and Tan X (2011) Fiber-directed conjugated-polymer torsional actuator: Nonlinear elasticity modeling and experimental validation. *IEEE/ASME Transactions on Mechatronics* 16(4): 656–664. DOI:10.1109/TMECH.2010.2049366.
- Galloway KC, Becker KP, Phillips B, Kirby J, Licht S, Tchernov D, Wood RJ and Gruber DF (2016) Soft robotic grippers for biological sampling on deep reefs. *Soft Robotics* 3(1): 23–33. DOI:10.1089/soro.2015.0019. URL <https://doi.org/10.1089/soro.2015.0019>. PMID: 27625917.
- Galloway KC, Chen Y, Templeton E, Rife B, Godage IS and Barth EJ (2019) Fiber optic shape sensing for soft robotics. *Soft Robotics* DOI:10.1089/soro.2018.0131. URL <https://www.liebertpub.com/doi/10.1089/soro.2018.0131>.
- Galloway KC, Polygerinos P, Walsh CJ and Wood RJ (2013) Mechanically programmable bend radius for fiber-reinforced soft actuators. In: *2013 16th International Conference on Advanced Robotics (ICAR)*. pp. 1–6. DOI:10.1109/ICAR.2013.6766586.
- Gosline JM and DeMont ME (1985) Jet-propelled swimming in squids. *Scientific American* 252: 96–103. DOI:10.1137/0911052. URL <http://dx.doi.org/10.1137/0911052>.
- Huang J, Lu T, Zhu J, Clarke DR and Suo Z (2012) Large, uni-directional actuation in dielectric elastomers achieved by fiber stiffening. *Applied physics letters* 100(21): 211901.
- Kier WM (1992) *Biomechanics (Structures and Systems): A Practical Approach*, chapter Hydrostatic skeletons and muscular hydrostats. Oxford, England: IRL Press at Oxford University, p. 11.
- Krieg M, Klein P, Hodgkinson R and Mohseni K (2011) A hybrid class underwater vehicle: Bioinspired propulsion, embedded system, and acoustic communication and localization system. *Marine Technology Society Journal: Special Edition on Biomimetics and Marine Technology* 45(4): 153–164. DOI:10.4031/MTSJ.45.4.11. URL <http://dx.doi.org/10.4031/MTSJ.45.4.11>.
- Krieg M and Mohseni K (2008) Thrust characterization of pulsatile vortex ring generators for locomotion of underwater robots. *IEEE Journal of Oceanic Engineering* 33(2): 123–132. DOI:10.1109/JOE.2008.920171. URL <http://dx.doi.org/10.1109/JOE.2008.920171>.
- Krieg M and Mohseni K (2010) Dynamic modeling and control of biologically inspired vortex ring thrusters for underwater robot locomotion. *IEEE Transactions on Robotics* 26(3): 542–554. DOI:10.1109/TRO.2010.2046069. URL <http://dx.doi.org/10.1109/TRO.2010.2046069>.
- Krieg M and Mohseni K (2012) New perspectives on collagen fibers in the squid mantle. *Journal of Morphology* 273(6): 586–595. DOI:10.1002/jmor.20003. URL <http://dx.doi.org/10.1002/jmor.20003>.
- Krieg M and Mohseni K (2017) Relative planar strain control and minimizing deformation work in elastomeric sheets via reinforcing fiber arrays. *Composites Science and Technology* 142: 50–64. DOI:http://dx.doi.org/10.1016/j.compscitech.2017.01.014. URL <http://www.sciencedirect.com/science/article/pii/S0266353816313021>.
- Krieg M, Nelson K, Eisele J and Mohseni K (2018) Bioinspired jet propulsion for disturbance rejection of marine robots. *IEEE Robotics and Automation Letters* 3(3): 2378–2385. DOI:10.1109/LRA.2018.2812219.
- Krieg M, Nelson K and Mohseni K (2019) Distributed environmental sensing for intelligent mobile robots. *Nature: Machine Intelligence* 1(5): 216–224. DOI:10.1038/s42256-019-0044-1.
- Laschi C, Mazzolai B and Cianchetti M (2016) Soft robotics: Technologies and systems pushing the boundaries of robot abilities. *Science Robotics* DOI:10.1126/scirobotics.aah3690.
- Lou S and Chou T (1988) Finite deformation and nonlinear elastic behavior of flexible composites. *Journal of Composite Materials* 55(1): 149–155. DOI:10.1115/1.3173621.
- Lou SY and Chou TW (1990) Finite deformation of flexible composites. *Proc. Roy. Soc. Lon. A* 429(1877): 569–586.
- Lu T, Huang J, Jordi C, Kovacs G, Huang R, Clarke DR and Suo Z (2012) Dielectric elastomer actuators under equal-biaxial forces, uniaxial forces, and uniaxial constraint of stiff fibers. *Soft Matter* 8(22): 6167–6173.
- Manti M, Cacucciolo V and Cianchetti M (2016) Stiffening in soft robotics: A review of the state of the art. *IEEE Robotics & Automation Magazine* 23: 93–106.
- Mather JA, Anderson RC and Wood JB (2010) *Octopus: The Ocean's Intelligent Invertebrate*. Timber Press.

- O'Dor RK and Webber DM (1991) Invertebrate athletes: Trade-offs between transport efficiency and power density in cephalopod evolution. *Journal of Experimental Biology* 160: 93–112.
- Peel LD (1998) *Fabrication and mechanics of fiber-reinforced elastomers*. PhD Thesis, Brigham Young University, Utah.
- Pikul JH, Li S, Bai H, Hanlon RT, Cohen I and Shepherd RF (2017) Stretchable surfaces with programmable 3d texture morphing for synthetic camouflaging skins. *Science* 358(6360): 210–214. DOI:10.1126/science.aan5627. URL <https://science.sciencemag.org/content/358/6360/210>.
- Polygerinos P, Correll N, Morin SA, Mosadegh B, Onal CD, Petersen K, Cianchetti M, Tolley MT and Shepherd RF (2017) Soft robotics: Review of fluid-driven intrinsically soft devices; manufacturing, sensing, control, and applications in human-robot interaction. *Advanced Engineering Materials* 19(12). DOI:10.1002/adem.201700016. URL <https://doi.org/10.1002/adem.201700016>.
- Rus D and Tolley M (2015) Design, fabrication and control of soft robots. *Nature* 521: 467–475.
- Shian S, Bertoldi K and Clarke DR (2015) Use of aligned fibers to enhance the performance of dielectric elastomer inchworm robots. In: *Electroactive Polymer Actuators and Devices (EAPAD) 2015*, volume 9430. International Society for Optics and Photonics, p. 94301P.
- Sholl N and Mohseni K (2019) A dual-bladder buoyancy engine for a cephalopod-inspired AUV. In: *Proceedings of the IEEE International Conference on Robotics and Automation (ICRA)*. Montreal, Canada.
- Sholl N, Moss A, Kier WM and Mohseni K (2019) A soft end effector inspired by cephalopod suckers and augmented by a dielectric elastomer actuator. *Soft Robotics* 6(3): 356–367. DOI:10.1089/soro.2018.0059.
- Song Z, Mazzola C, Schwartz E, Finlaw J, Chen R, Krieg M and Mohseni K (2016) A compact autonomous underwater vehicle with cephalopod-inspired propulsion. *Marine Technology Society Journal* 50(5): 88–101. DOI:10.4031/MTSJ.50.5.9. URL <http://dx.doi.org/10.4031/MTSJ.50.5.9>.
- Tavakoli M, Rocha RP, Lourenço J, Lu T and Majidi C (2017) Soft bionics hands with a sense of touch through an electronic skin. *Soft Robotics: Trends, Applications and Challenges* : 5–10.
- Trivedi D, Rahn CD, Kier WM and Walker ID (2008) Soft robotics: Biological inspiration, state of the art, and future research. *Applied Bionics and Biomechanics* 5(3): 99–117. DOI:10.1080/11762320802557865. URL <http://dx.doi.org/10.1080/11762320802557865>.
- Wainwright SA, Biggs WD, Currey JD and Gosline JM (1976) *Mechanical Design in Organisms*. Princeton, NJ, USA: Princeton University Press. ISBN 978-0691083087.
- Ward DV and Wainwright SA (1972) Locomotory aspects of squid mantle structure. *Journal of Zoology* 167(4): 437–449. DOI:10.1111/j.1469-7998.1972.tb01735.x. URL <http://dx.doi.org/10.1111/j.1469-7998.1972.tb01735.x>.